Supplementary Information

Room-temperature electronic ferroelectricity in monolayer graphene on Fe_2O_3 film

Kyunghwan Sung[1], Qi Zhang[2], Yongjoon Kwon[1], Hyobin Nam[3], Kenji Watanabe[4], Takashi Taniguchi[4], Sung-Jin Chang[5], Chanho Yang[1], Seungyong Lee[3], Euyheon Hwang[2], and Sungjae Cho[1]

[1] Department of Physics, Korea Advanced Institute of Science and Technology (KAIST), Daejeon, Republic of Korea

[2] SKKU Advanced Institute of Nanotechnology (SAINT), Sungkyunkwan University (SKKU), Suwon, Republic of Korea

[3] Materials Architecturing Research Center, Korea Institute of Science and Technology, Seoul, Republic of Korea

[4] National Institute for Materials Science, Namiki Tsukuba Ibaraki 305-0044, Japan

[5] Center for Analysis and Evaluation, National Nanofab Center, Daejeon, Republic of Korea

Supplementary Texts

1. Candidates for hysteresis

To claim that the hysteresis observed in gate sweep originates from ferroelectricity, it is essential to first clarify that the hysteresis does not stem from other possible mechanisms. One possible origin of the hysteresis is charge trapping at the graphene layer. Charge impurities originating from adsorbates adhered to the graphene surface during the fabrication process can induce charge trapping or capacitive gating effects [1]. The shift of the charge neutrality point (CNP) toward the positive (negative) direction during the gate backward scan is associated with charge trapping (capacitive gating). These two effects arise from charge impurities locally inducing an unbalanced potential distribution in graphene. This unbalanced distribution is not permanent but instead exhibits relaxation time, which is closely related to the sweeping rate of the gate voltage. Therefore, the resulting hysteresis strongly depends on the sweeping rate, showing a tendency to decrease as the sweep rate becomes lower (Supplementary Figure S1a).

Our device exhibits negligible hysteresis during the V_{TG} sweep, indicating that the upper surface of the graphene is largely free from factors inducing charge trapping. Still, there remains a possibility of charge trap on the lower surface of the graphene, so we conducted measurements while varying the scan rate of the bottom gate sweep, as shown in Supplementary Figure S1b. Since charge trapping is not strongly dependent on the sweeping gate range, the measurements were conducted by fixing the gate range to a specific value where the hysteresis is clearly observed. The large hysteresis observed during the forward and backward scans from V_{BG} = 60 V to -60 V shows little variation in both the positions of the CNP and the peak intensities, even when the sweep rate is increased by a factor of eight. This indicates that the hysteresis is nearly independent of the scan rate, which strongly suggests that the origin of the hysteresis is unlikely to be related to the charge trapping effects.

Next, it is important to consider that hysteresis can also appear when graphene detects the polarization switching of a ferroelectric material. As demonstrated in previous studies on the ferroelectricity of multilayer 1T' WTe_2 [2] and parallel-stacked bilayer hBN [3, 4], the high sensitivity to external electric field of graphene allows it to serve as a detector for ferroelectric switching in adjacent materials. Therefore, it is crucial to verify that the Fe_2O_3 layer between the graphene and the bottom gate is non-ferroelectric. Without this verification,

it would be difficult to rule out the possibility that the observed hysteresis in the main text is a trivial ferroelectricity of the Fe_2O_3 layer detected by graphene.

Fe_2O_3 can exhibit various structural phases depending on the O_2/Fe ratio. Among these, α-Fe_2O_3, the most common phase found in nature, is known to exhibit nearly zero ferroelectricity [5], whereas ε-Fe_2O_3 has been reported to exhibit ferroelectric properties [6]. Therefore, it is of critical importance to directly confirm whether the Fe_2O_3 used in our system is ferroelectric or not. We employed piezoresponse force microscopy (PFM) measurements to determine whether Fe_2O_3 without graphene exhibits ferroelectricity. Before conducting the PFM measurements, we checked the sample thickness near the edge of the untreated pure Fe_2O_3 sample (Supplementary Figure S2a). Additionally, we performed further measurements to investigate the presence of domains in both out-of-plane and in-plane directions. However, it was difficult to observe any significant signals in both directions.

Additionally, it can be confirmed through Raman spectroscopy that which type of Fe_2O_3 is used in our system. α-Fe_2O_3 and ε-Fe_2O_3 exhibit distinct Raman peak characteristics [7]. When Raman measurements are performed using a 532 nm laser, α-Fe_2O_3 shows strong peaks at 411 cm^{-1} and 1320 cm^{-1}, whereas ε-Fe_2O_3 shows strong peaks at 325 cm^{-1} and 685 cm^{-1}. As shown in Supplementary Figure S3, comparing the Raman peaks of the SiO_2/Si substrate with those of the Fe_2O_3 film on the substrate, we observe peaks at 405 cm^{-1} and 1313 cm^{-1}, which correspond to the Raman characteristics of α-Fe_2O_3.

It is extensively established from previous studies that MLG itself is not ferroelectric, and bulk hBN also forms an AA' stacking order, which does not exhibit polarization switching [3]. Therefore, we can argue ferroelectricity is observed in the system despite all the materials used being non-ferroelectric. The possibility of a doubly aligned configuration between MLG and hBN is also unlikely, as we carefully misaligned MLG and hBN. The fact that no second Dirac point is observed also supports there is no moiré superlattice on graphene layer. Therefore, the remaining possibility is that the ferroelectricity is induced by the interaction between MLG and Fe_2O_3 film, which will be discussed in detail in the following section.

2. Origin of electronic ferroelectricity

The observed data exhibit characteristics of unconventional ferroelectricity, specifically electronically driven ferroelectricity. In this mechanism, the hysteresis in resistance arises from charge transfer between graphene and the Fe_2O_3 layer. This charge-transfer-induced dipole switching provides a natural explanation for the ferroelectric-like hysteresis observed in the device.

The charge transfer between graphene and the Fe_2O_3 layer is attributed to thermionic-field emission, (i.e., Fowler–Nordheim (FN) tunneling), through which electrons or holes are injected from the graphene into the Fe_2O_3 layer. Supplementary Figure S4 presents the energy band diagram of the device. At room temperature, thermally excited electrons and holes exist in the graphene. When V_{BG} is zero, the graphene remains electrically neutral, and the electric field across the hBN dielectric layer, E_{hBN}, is negligible. Due to the sufficiently large thickness and high potential barrier of the hBN, these thermally excited carriers cannot overcome the barrier, and consequently, no significant thermionic or tunneling current reaches the Fe_2O_3 film under zero-gate conditions.

On the other hand, as shown in Supplementary Figure S5, the application of a sufficiently large positive V_{BG} changes the band profile. The increase in E_{hBN} reduces the effective tunneling width of the potential barrier, allowing thermionic-field emission of electrons from graphene into the Fe_2O_3 film. Conversely, as shown in Supplementary Figure S6, applying a sufficiently large negative V_{BG} results in a large negative E_{hBN}, which similarly thins the potential barrier and enables thermionic-field emission of holes from graphene to Fe_2O_3. To quantitatively evaluate the carrier density that undergoes tunneling and to explain why n_H remains constant during monotonic sweeps of V_{BG}, a detailed analysis of the tunneling current and carrier dynamics is required.

Supplementary Figure S7b illustrates the band diagram of the device during process i. At this stage, the bottom gate voltage is set to $V_{BG} = V_0$, and the induced charge in the silicon substrate is Q_0. The corresponding electric field across the hBN dielectric is E_0, and thus, an equal and opposite charge, $-Q_0$, is induced on the graphene layer. Since the graphene is grounded during the measurement, its potential is set to zero. As shown in Supplementary Figure S7b, applying Gauss's law to a Gaussian surface of area A yields the relation $E_0 = Q_0/\varepsilon A$. At this point, the potential barrier of the hBN remains sufficiently thick to prevent FN tunneling. However, when the electric field is increased slightly beyond this point, electrons in the graphene layer begin to tunnel through the hBN barrier.

Supplementary Figure S8 illustrates the evolution of charge distribution, potential, and electric field upon a slight increase in V_{BG}. When V_{BG} is increased from V_0 to $V_0+\alpha V_0$, the induced charge in the silicon substrate becomes $Q_0+\alpha Q_0$, the electric field across the hBN layer becomes $E_0+\alpha E_0$, and the charge induced in the graphene is $-Q_0-\alpha Q$. As the field across the hBN increases, FN tunneling occurs, i.e., the thermionic field emission allows electrons in the graphene to tunnel into the Fe_2O_3 layer, as shown in Supplementary Figure S8c. If we denote the resulting charge changes in the silicon substrate, graphene, and Fe_2O_3 as $p\beta Q_0$, $q\beta Q_0$, and $-\beta Q_0$ respectively, then by Gauss's law applied to Gaussian surface 1, we obtain the relation $p+q = 1$. Let ΔE denote the change in the electric field across hBN during the tunneling process. FN tunneling continues until the field returns to E_0. Applying Gauss's law to Gaussian surface 2 gives:

$$(1+\alpha)E_0 + \Delta E = \frac{Q_0}{\varepsilon A}(1+\alpha-q\beta) = E_0.$$

Solving this yields $\Delta E = -\alpha E_0$ and $\alpha=q\beta$. Therefore, regardless of the amount of charge trapped in the Fe_2O_3 layer, the induced charge on graphene remains constant at $-Q_0$. This mechanism accounts for the observation that the Hall carrier density in graphene remains unchanged while V_{BG} increases from process (i) to (ii). A similar argument explains the invariance of n_H during the decrease of V_{BG} as well. Using the known thicknesses and dielectric constants of SiO_2 and hBN layers, the parameter β can be expressed explicitly as a function of α. This relation enables a quantitative estimate of the amount of charge transferred from the graphene layer into Fe_2O_3. However, because this charge-transfer process cannot be directly probed using conventional transport measurements, we do not pursue a more detailed analysis here.

As described in the main text, the Hall measurements shown in Supplementary Figure S9a, S9b are divided into eight stages, from Process (i) to Process (viii). The charge distribution on the surfaces of graphene and Fe_2O_3 at each process is schematically illustrated in Supplementary Figure S9c.

In Process (i), when a positive V_{BG} is weakly applied, electrons are typically induced on graphene. As the process transitions from (i) to (ii), upon further increase of V_{BG}, E_{hBN} surpasses the critical threshold, resulting in thermionic-field emission that facilitates the transfer of electrons from graphene to the Fe_2O_3 film. As a result, the Hall carrier density (n_H) remains constant, while the transferred carrier density (n_{tr}) increases. In the

transition from Process (ii) to (iii), when V_{BG} is decreased, electrons in graphene are typically removed to become zero. When V_{BG} decreases further, holes are typically induced on graphene, as shown in Process (iv).

In the transition from Process (iv) to (vi), upon further decrease of V_{BG}, E_{hBN} surpasses the critical threshold again, resulting in the transfer of holes from graphene to the Fe_2O_3 film. In the transition from Process (vi) to (vii), when V_{BG} increases again, holes in graphene are typically removed to become zero. When V_{BG} increases further, electrons are typically induced on graphene, as shown in Process (viii).

This picture clearly explains why our system exhibits a clockwise polarization, unlike typical ferroelectric materials, and how, in contrast to previous electronic ferroelectric systems, the n_{tr} value continues to increase beyond the half-filling of the Gr/hBN superlattice without saturation.

3. Scan range-dependence of hysteresis loop

In conventional and interfacial ferroelectrics, there exists a constant coercive field, which is the minimum displacement field (D) strength required for ferroelectricity to emerge. However, in the case of electronic ferroelectrics, the amplitude of the field which ferroelectric hysteresis begins to appear, or equivalently, the V_{BG} value which GSAS begins to emerge, is not fixed. This characteristic can also be observed in our system, as shown in Figure 2 in the main text, where the V_{BG} value at which Coulomb screening appears increases at the same rate as the range of the V_{BG} sweep increases.

The V_{BG} value can change not only with respect to the sweep range but also with respect to the sweep history. In the dual gate sweep, when the V_{BG} scan rate is limited to 60 V to -20 V, screening appears at 34 V for the V_{BG} backward scan and 4 V for the V_{BG} forward scan (Supplementary Figure S10a, S10b). On the other hand, when the V_{BG} scan rate is measured from 20 V to -60 V, screening appears at -2 V for the V_{BG} backward scan and -31 V for the V_{BG} forward scan (Supplementary Figure S10d, S10e). This indicates that, despite sweeping the same range of V_{BG}, the V_{BG} value which screening begins to appear can vary depending on which V_{BG} value is swept, and accordingly, the position of the hysteresis loop can shift (Supplementary Figure S10c, S10f).

4. Independence of hysteretic behavior of the slow scan direction

As mentioned in Figure 2 of the main text, the V_{TG} sweep has little effect on the formation of hysteresis. Another method to verify this is by swapping the V_{TG} and V_{BG} scan axes and performing a dual gate sweep. As shown in Supplementary Figure S11, even when the scan axes are swapped, the normal graphene behavior regime and screening regime are observed in the same form as in Figure 1 of the main text. In the V_{BG} downward scan, screening begins to appear at 32.5 V, and in forward scan, screening begins at -32.5 V, which almost exactly matches the values observed during the V_{BG} slow scan, 34 V, -33 V. Supplementary Figure S11a and S11d, as well as S11b and S11e, only differ in the direction of the V_{TG} slow scan, but the results are almost identical. This supports the independence of hysteresis of the V_{TG} sweep.

5. Temperature dependence of electronic ferroelectricity

The electronic ferroelectricity observed in graphene-hBN moiré superlattice shows that as the temperature increases, a portion of the localized charges becomes thermally excited and exhibits itinerant behavior [8]. As a result, the strength of the electron-hole dipole weakens with increasing temperature, and consequently, the ferroelectric strength also diminishes. In contrast, our system, which does not exhibit a moiré superlattice, shows a significant difference in temperature dependence. As seen in Supplementary Figure S12a, S12b, the R_{xx} peak hysteresis and screening behavior are not observed at low temperatures. However, ferroelectricity begins to appear, grow, and saturate as the temperature gradually increases.

Supplementary Figure S12c, S12d plot the V_{BG} difference of CNPs and the remanent Hall carrier density as a function of temperature, respectively, extracted from Supplementary Figure S12a, S12b. Both variables are close to zero at temperatures below 100 K. They gradually increase from 115 K to 175 K, and converge to a constant value from 175 K to room temperature. This behavior is also confirmed by the low-temperature dual gate sweep measurements in Supplementary Figure S13. At 125 K, the ferroelectric polarization strength is weak, resulting in a small loop size. At 200 K, the loop size is almost the same as at room temperature. This can be interpreted as transferred carriers being more pronounced at higher temperatures, suggesting that a different mechanism from previous reports for electronic ferroelectricity is at play.

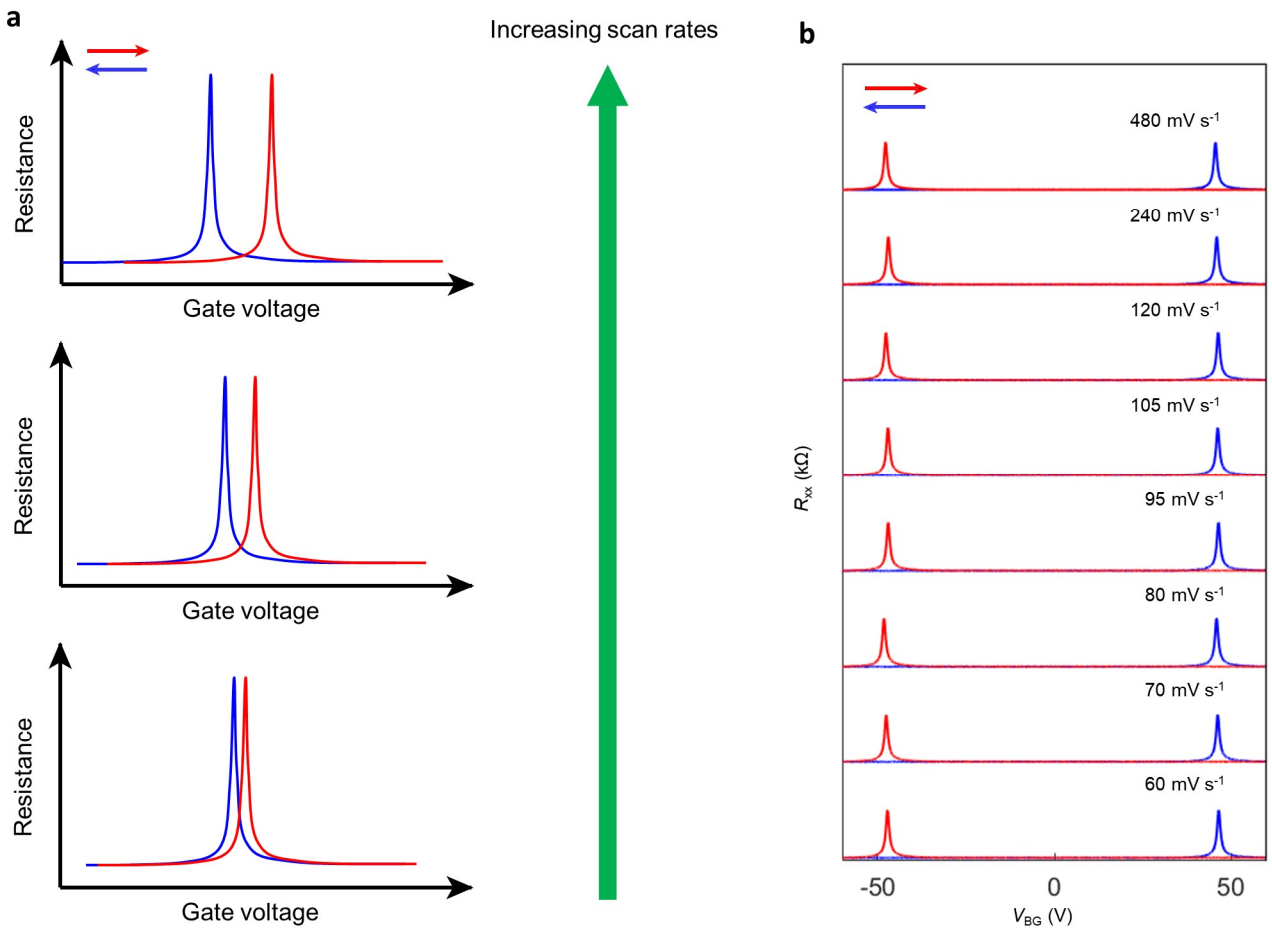

Supplementary Fig. S1 Hysteresis scan with various scan rates. a, Schematic of typical hysteresis originated from charge trap on measurement of resistance of graphene. From bottom to top, the magnitude of hysteresis gets larger with increasing scan rates. **b**, R_{xx} by scanning V_{BG} forward (red) and backward (blue) at a fixed $V_{TG} = 0$. The curves are vertically shifted for clarity. There are little differences among scan rates from 60 mV s^{-1} to 480 mV s^{-1}.

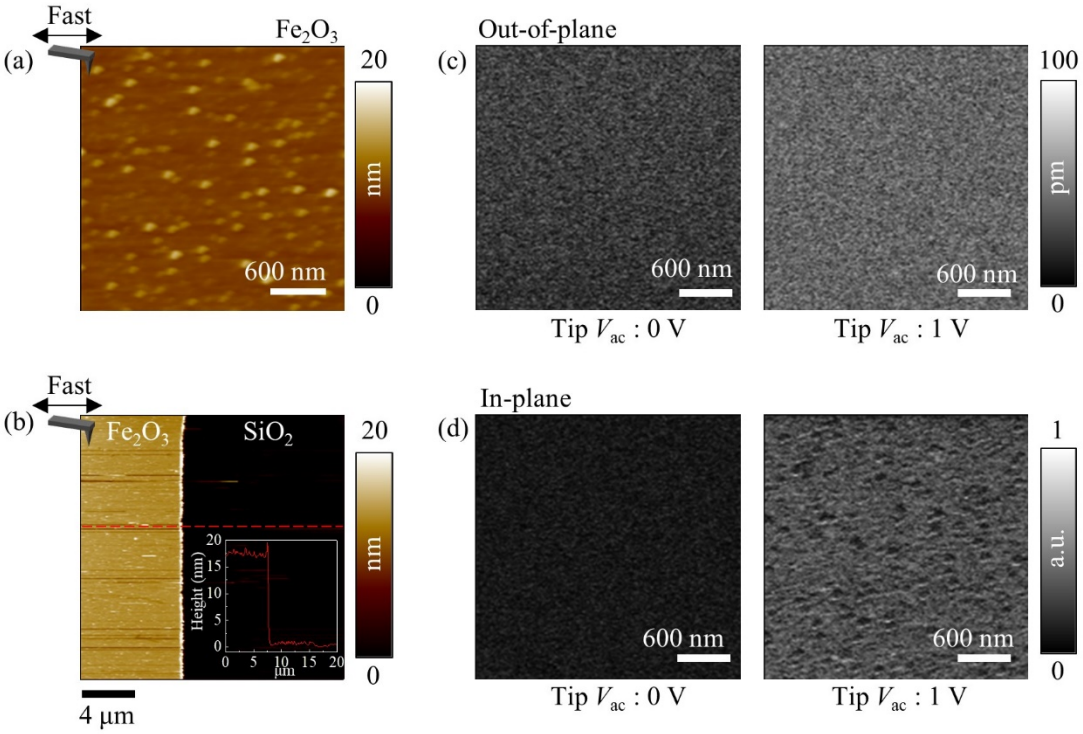

Supplementary Fig. S2 Piezoresponse force microscopy measurement of the sample without the graphene. a, **b**, Surface topography of the Fe_2O_3 (**a**) and in the region of the edge of Fe_2O_3 (**b**). The inset shows that the thickness of the Fe_2O_3 is approximately 17.5 nm, as indicated by the red dashed line. PFM amplitude images of the out-of-plane (**c**) and in-plane (**d**) were acquired in the area shown in (**a**). Ferroelectric domains are not clearly observed. All measurements were conducted at room temperature.

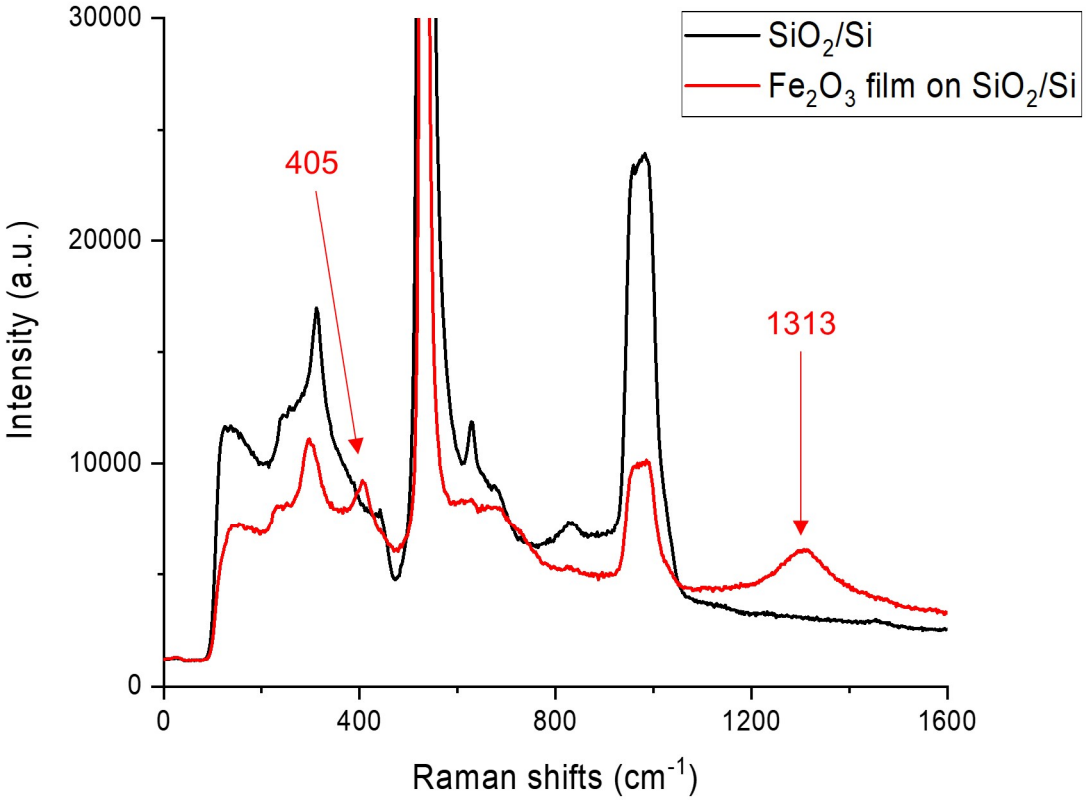

Supplementary Fig. S3 Raman spectroscopy of Fe_2O_3 film. Comparison of Raman spectra acquired in SiO_2/Si and Fe_2O_3 film on SiO_2/Si.

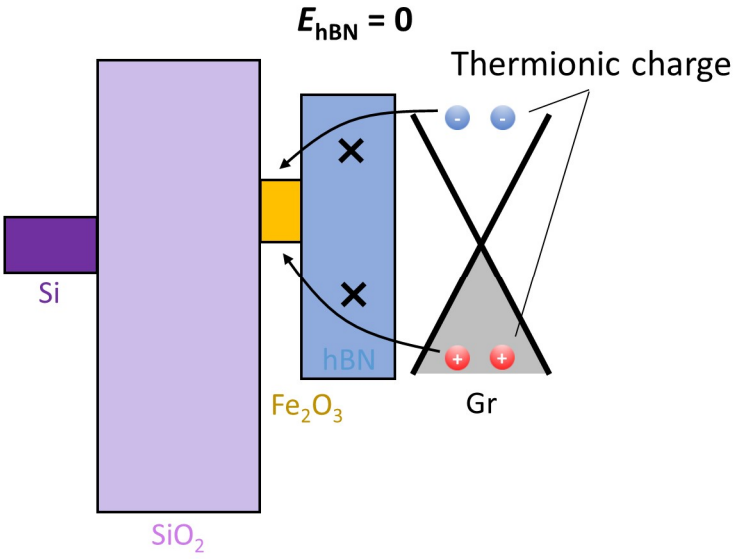

Supplementary Fig. S4 Band diagram of the device (zero E_{hBN}). Schematic illustration showing how charges from graphene can move to Fe_2O_3 film. The blue (red) circles denote thermionic electrons (holes). V_{TG} is not included because graphene screens its electric field effect through the bottom hBN.

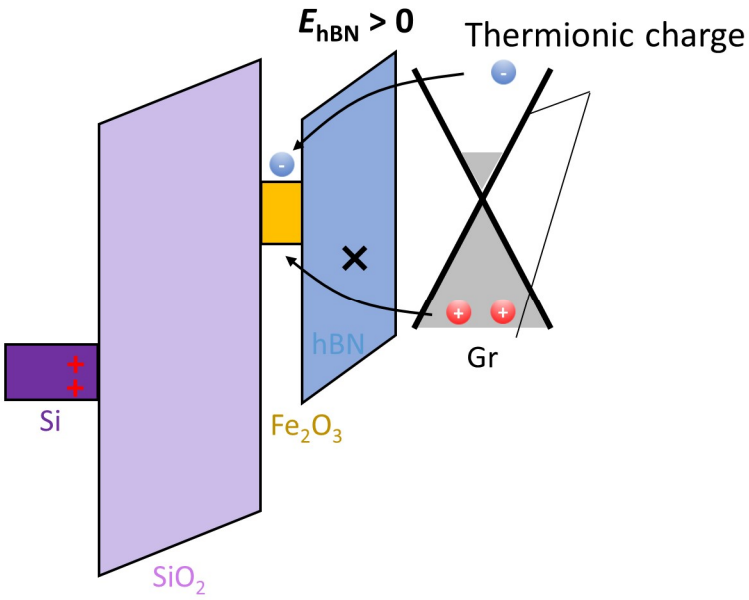

Supplementary Fig. S5 Band diagram of the device (positive E_{hBN}). Schematic illustration showing how charges from graphene can move to Fe_2O_3 film. The blue (red) circles denote thermionic electrons (holes). V_{TG} is not included because graphene screens its electric field effect through the bottom hBN.

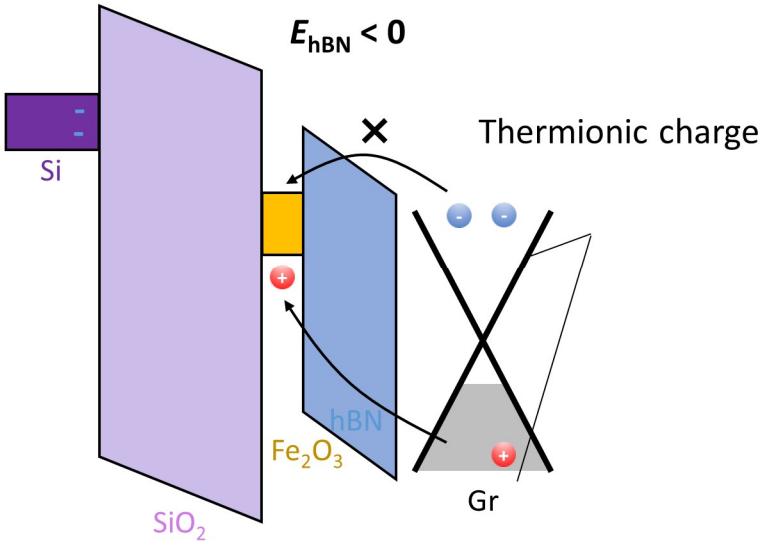

Supplementary Fig. S6 Band diagram of the device (negative E_{hBN}). Schematic illustration showing how charges from graphene can move to Fe_2O_3 film. The blue (red) circles denote thermionic electrons (holes). V_{TG} is not included because graphene screens its electric field effect through the bottom hBN.

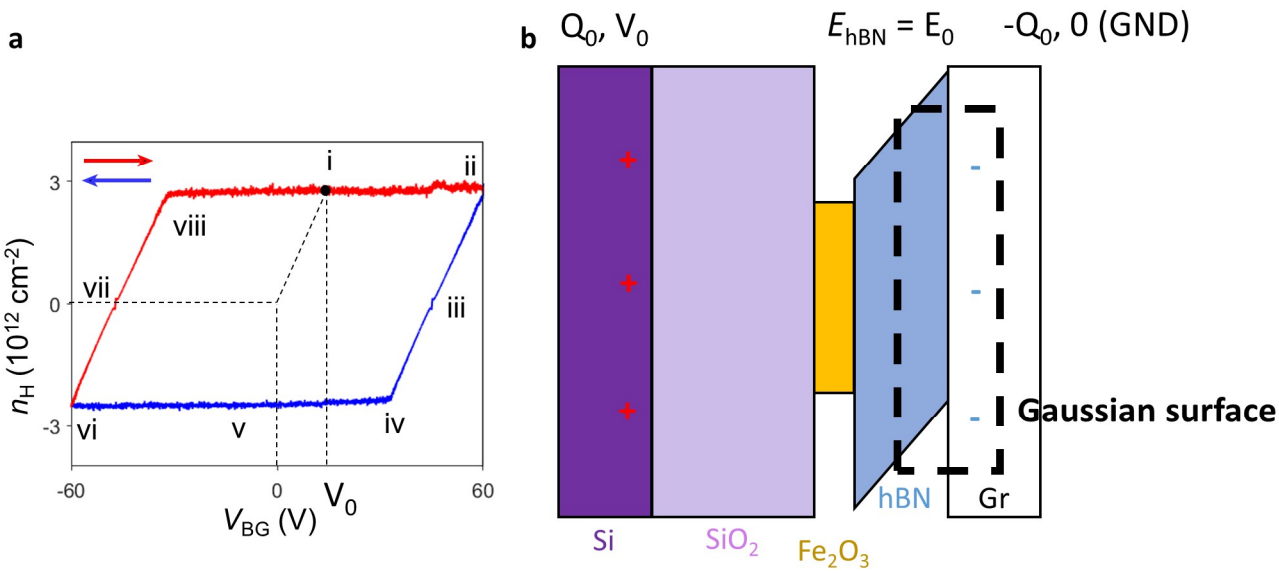

Supplementary Fig. S7 Band diagram of the device (increasing V_{BG}). a, n_H measurement data showing the screening regime. **b,** Schematic illustration showing how electrons from graphene can move to Fe_2O_3 film. V_{TG} is not included because graphene screens its electric field effect through the bottom hBN.

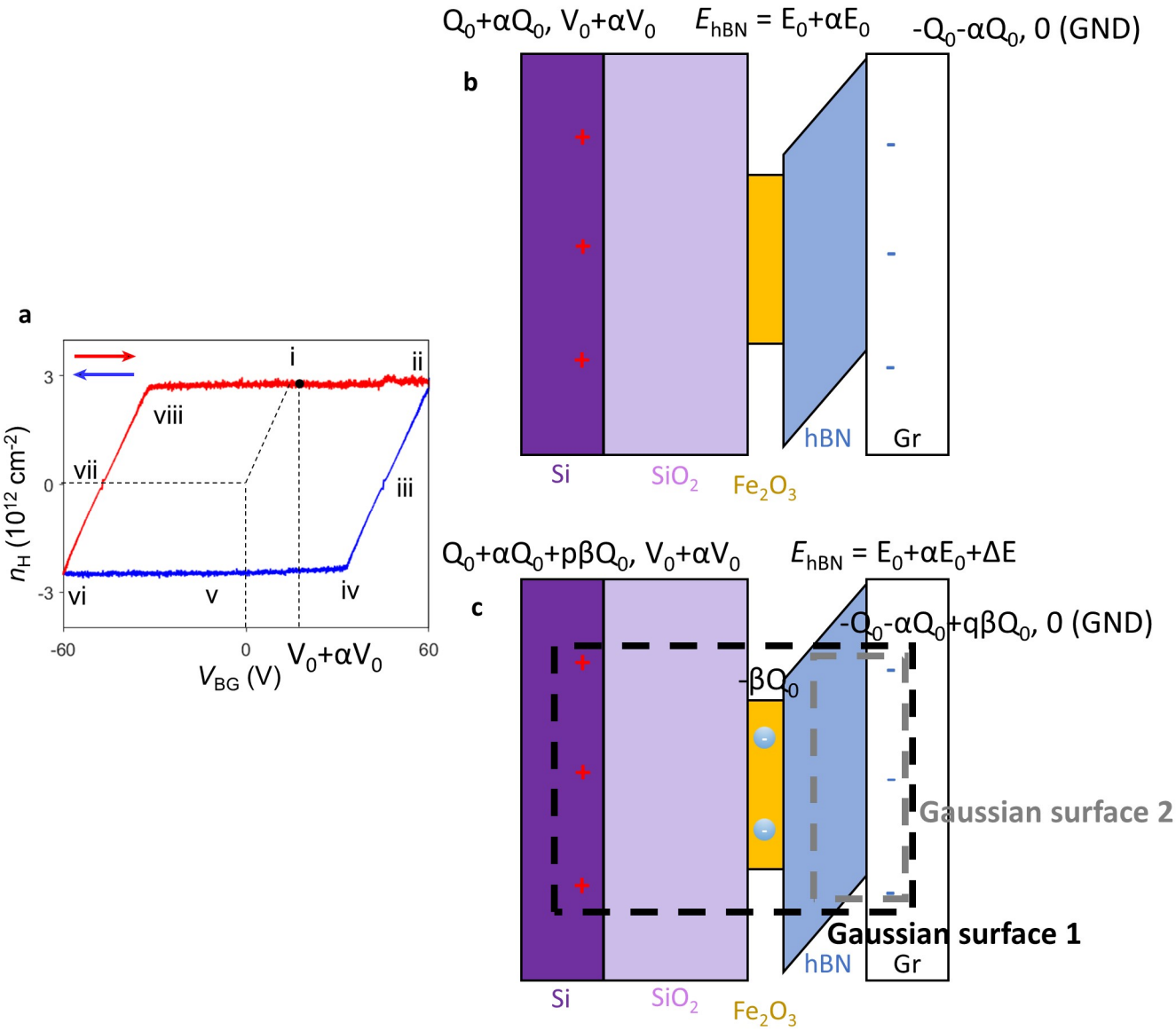

Supplementary Fig. S8 Band diagram of the device (increasing V_{BG}). a, n_H measurement data showing the screening regime. **b,** Schematic illustration showing the moment E_{hBN} is increased to cause FN tunneling. **c,** Schematic illustration showing the moment that thermionic electrons from the graphene move to the Fe_2O_3 film. The blue circles denote thermionic electrons. V_{TG} is not included because graphene screens its electric field effect through the bottom hBN.

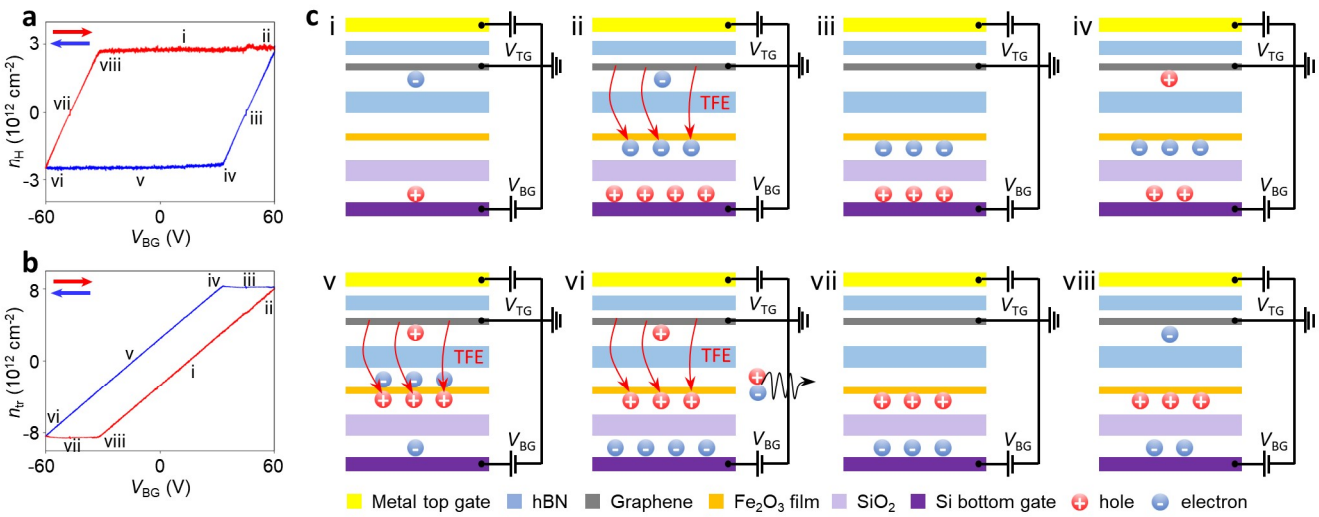

Supplementary Fig. S9 Schematic of formation of Hall and transferred charges explaining the origin of ferroelectricity. a, **b**, Hall (a) and transferred (b) carrier density when scanning V_{BG} backward (blue) and forward (red) at fixed V_{TG} = 0. **c**, Schematic of charge carrier on monolayer graphene, Fe_2O_3 film, and Si bottom gate when applying bottom gate voltage for each process (i)-(viii). The red arrows denote thermionic-field emission (TFE). The black wavy arrow denotes the recombination of electrons and holes.

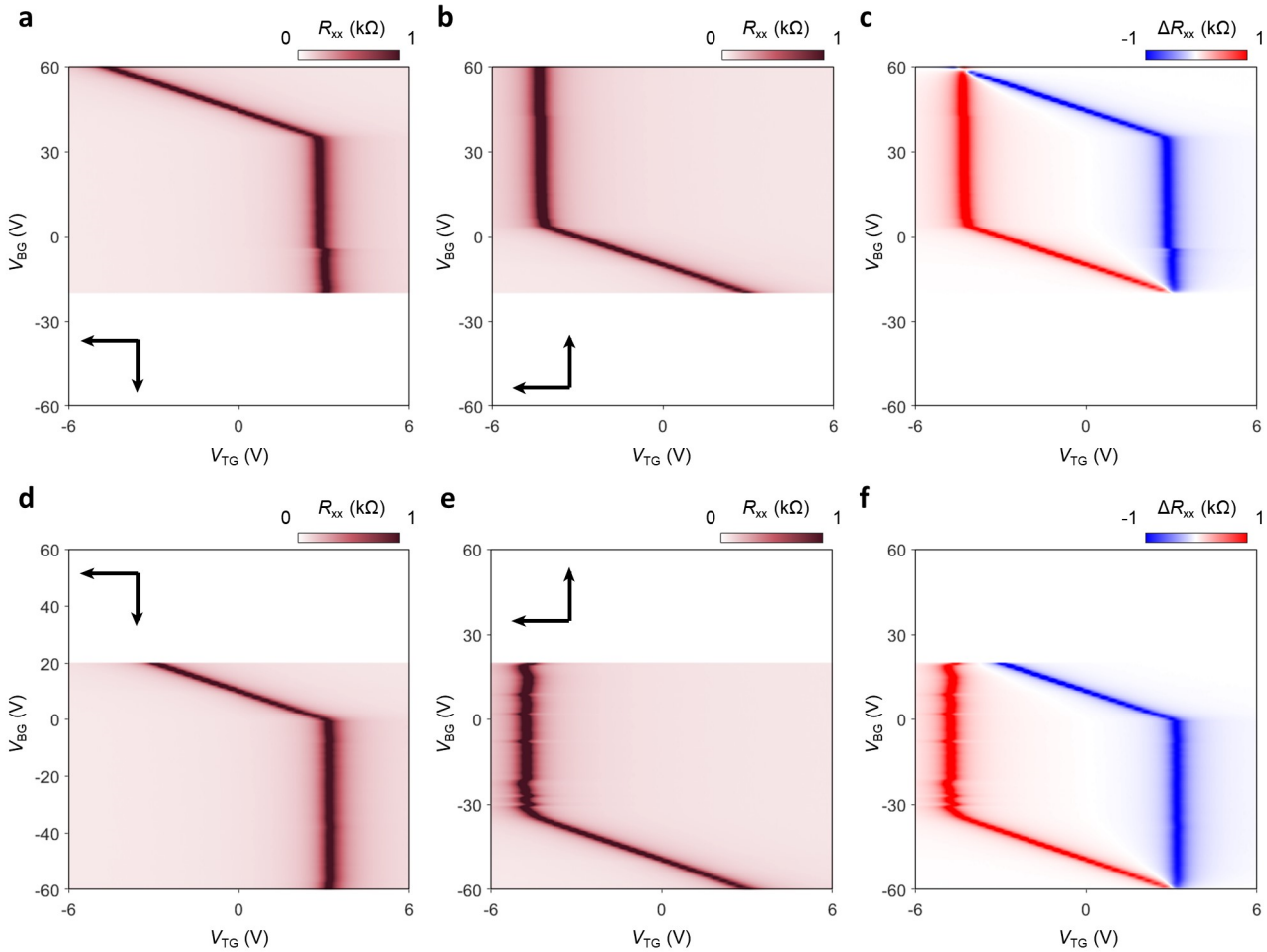

Supplementary Fig. S10 Shift of hysteresis loop depending on the range of V_{BG}. a-c, Backward (**a**) and forward (**b**) V_{BG} slow scan of R_{xx} when fast scanning V_{TG} and their difference (**c**). The scan range of V_{BG} is from -20 V to 60 V. **d-f**, Same with **a-c**, except that the range of V_{BG} is from -60 V to 20 V.

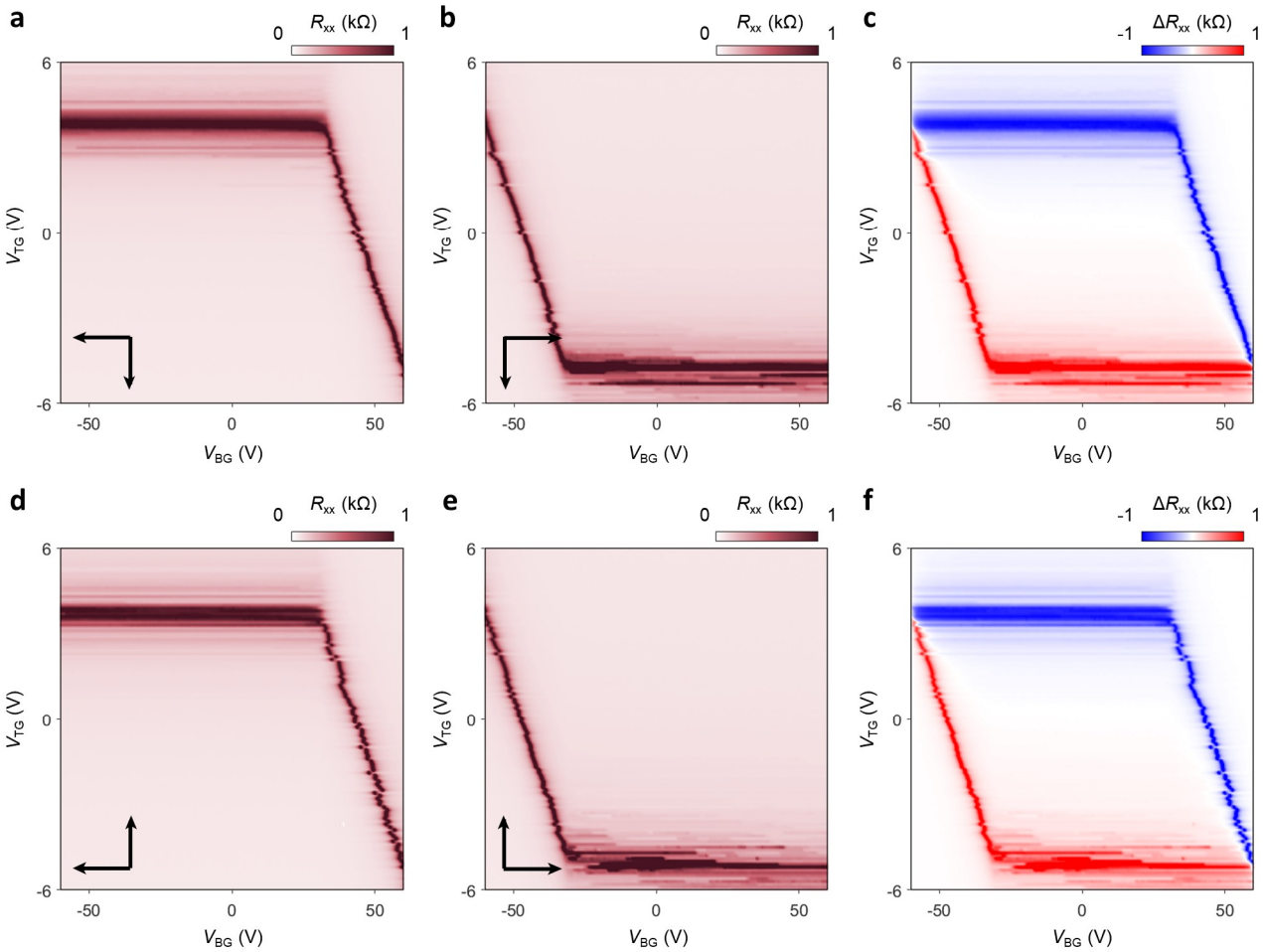

Supplementary Fig. S11 All scanning configurations when fast scan and slow scan axes swapped. **a-c**, Backward (**a**) and forward (**b**) V_{BG} fast scan of R_{xx} when slow backward scanning V_{TG} and their difference (**c**). **d-f**, Same with **a-c**, except that V_{TG} scan is in forward direction.

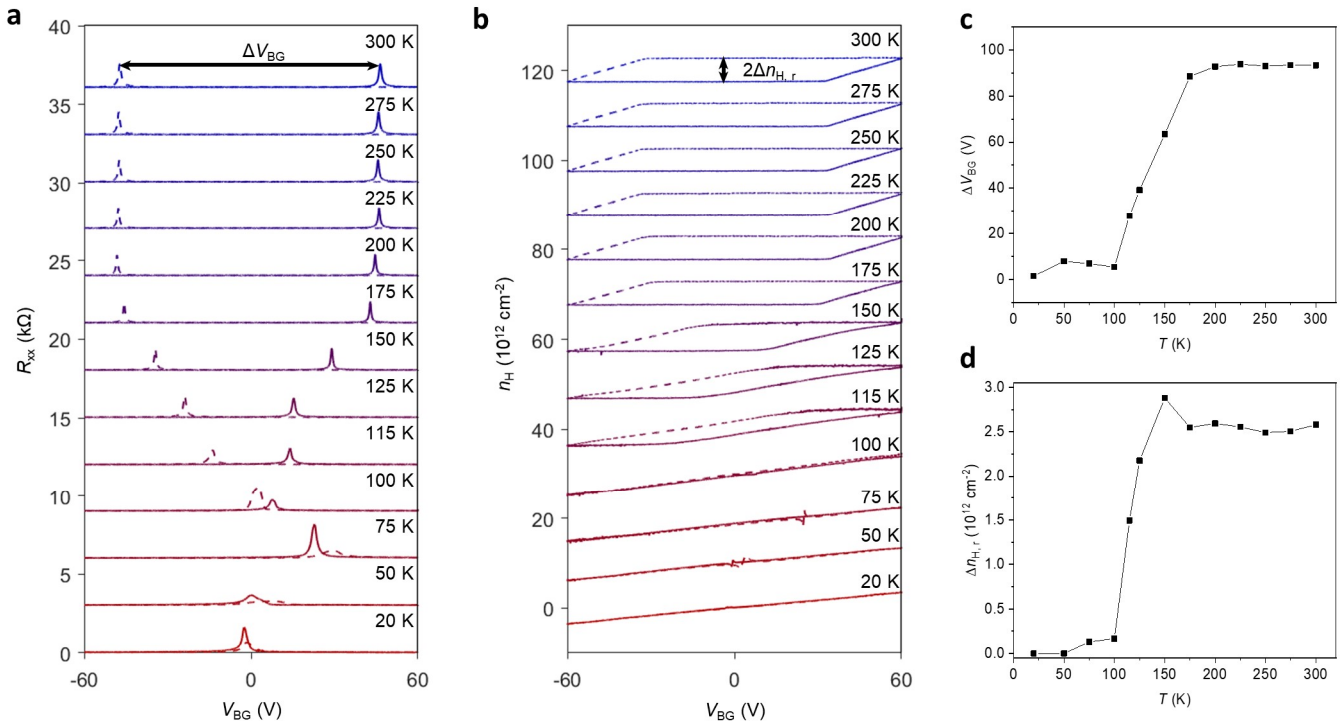

Supplementary Fig. S12 Temperature dependence of ferroelectricity. a, **b**, Longitudinal resistance (**a**) and Hall carrier density (**b**) when scanning V_{BG} backward (solid lines) and forward (dashed lines) directions at V_{TG} = 0, measured at various temperatures. The curves are vertically shifted for clarity. **c**, **d**, The V_{BG} difference of charge neutrality points (**c**) and remanent Hall carrier density (**d**) as a function of temperature.

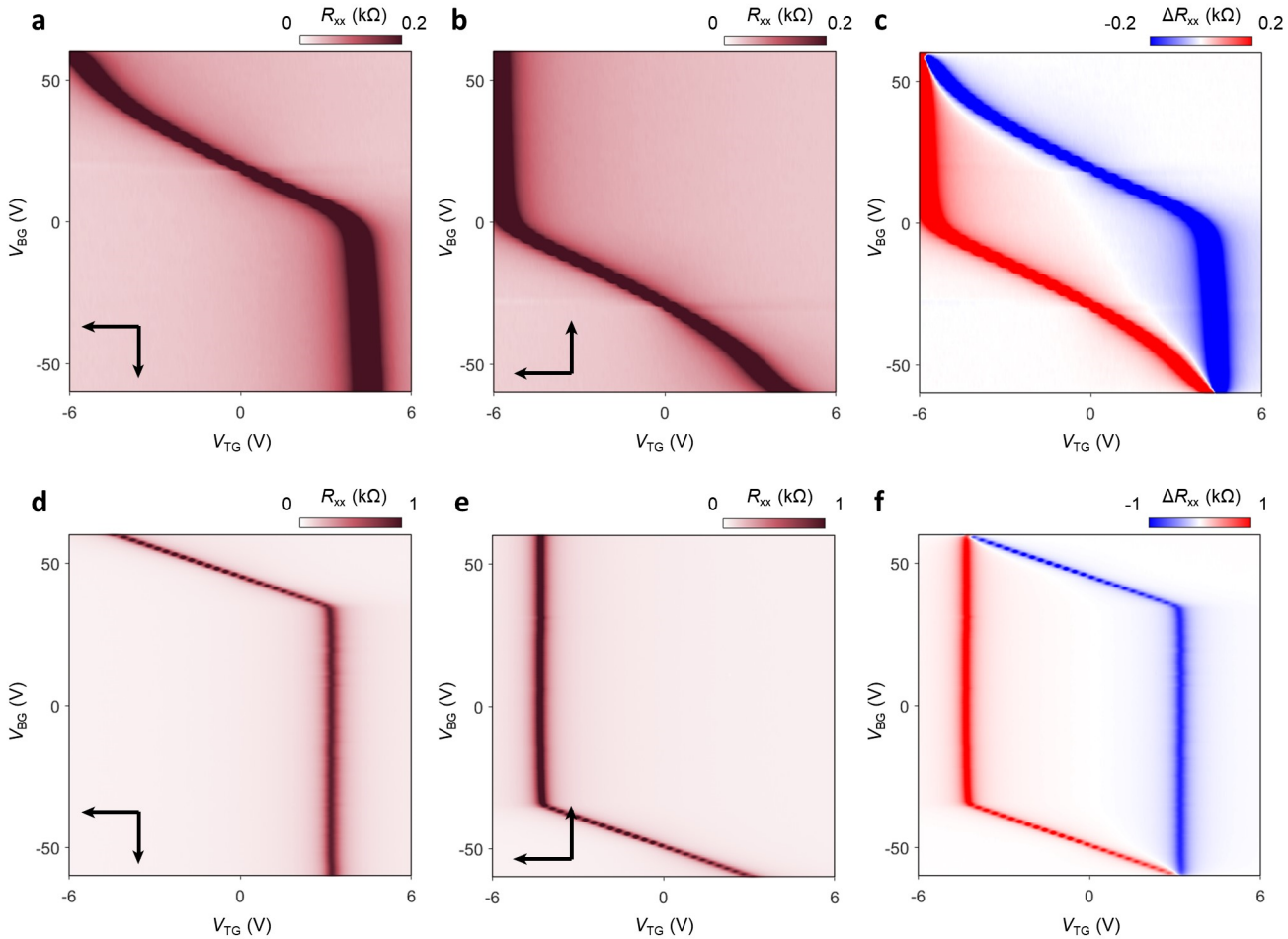

Supplementary Fig. S13 Hysteresis loops characterized at low temperatures. a-c, Backward (**a**) and forward (**b**) V_{BG} fast scan of R_{xx} when slow backward scanning V_{TG} and their difference (**c**), measured at T = 125 K. **d-f**, Same with **a-c**, except that T = 200 K.

Supplementary references

[1] Wang, H., Wu, Y., Cong, C., Shang, J. & Yu, T. Hysteresis of electronic transport in graphene transistors. ACS nano 4, 7221–7228 (2010).

[2] Fei, Z. et al. Ferroelectric switching of a two-dimensional metal. Nature 560, 336–339 (2018).

[3] Yasuda, K., Wang, X., Watanabe, K., Taniguchi, T. & Jarillo-Herrero, P. Stacking-engineered ferroelectricity in bilayer boron nitride. Science 372, 1458–1462 (2021).

[4] Yasuda, K. et al. Ultrafast high-endurance memory based on sliding ferroelectrics. Science 385, 53–56 (2024).

[5] Ma, Z. et al. Novel magnetic and ferroelectric behaviors observed in alpha Fe2O3 particles. Preprint at https://doi.org/10.48550/arXiv.2009.09199 (2020).

[6] Hamasaki, Y. et al. Ferroelectric and magnetic properties in ε-Fe2O3 epitaxial film. Applied Physics Letters 119, 182904 (2021).

[7] Zhao, Z. et al. A general thermodynamics-triggered competitive growth model to guide the synthesis of two-dimensional nonlayered materials. Nat Commun 14, 958 (2023).

[8] Zhang, L. et al. Electronic ferroelectricity in monolayer graphene moiré superlattices. Nat Commun 15, 10905 (2024).